colloids and interfaces

MDPI

Article

Microfluidic Evaluation of Oil Recovery Efficiency Using Magnesium Oxide Nanoparticle Suspensions Synthesized by Sol–Gel Method

Maxim Pryazhnikov, Hedi Ben Ahmed, Andrey Pryazhnikov, Sofia Kazanina, Roman Vaganov, Vladimir Zhigarev * and Andrey Minakov *

Laboratory of Physical and Chemical Technologies for the Development of Hard-to-Recover Hydrocarbon Reserve, Siberian Federal University, Krasnoyarsk 660041, Russia; benahmedhedi93@gmail.com (H.B.A.)
* Correspondence: vzhigarev@sfu-kras.ru (V.Z.); tov-andrey@yandex.ru (A.M.)

Abstract

For the first time, a systematic study was conducted on the properties and colloidal stability of suspensions containing synthesized MgO nanoparticles. The nanoparticles were synthesized using hydroquinone as a chelating agent. This approach ensured the formation of an ultradispersed system with an average size of 14 nm and also prevented the formation of stable micrometer-sized agglomerates, as confirmed by acoustic spectroscopy data. The suspensions were characterized for colloidal stability, rheological properties, and surface properties. Light transmission profiles along the height of the sample remained virtually unchanged. Rheological measurements demonstrated Newtonian flow patterns across the entire concentration range studied. The surface tension of the suspensions at the air interface remained at the level of distilled water (72–73 mN/m), indicating the absence of pronounced particle surface activity. A microfluidic study was conducted to evaluate the efficiency of oil displacement from a model pore space using suspensions of synthesized nanoparticles stabilized with hydroquinone. The displacement efficiency consistently increased with increasing MgO concentration. For water, it was 44.15%, reaching 55% at 2 wt.% nanoparticles. The results demonstrate the potential of MgO suspensions synthesized with hydroquinone for enhanced oil recovery technologies.

Keywords: sol–gel method; MgO nanoparticles; nanosuspension; colloidal stability; viscosity; microfluidics; enhanced oil recovery

Check for updates

Academic Editor: Plamen Tchoukov

Received: 18 August 2026
Revised: 21 September 2026
Accepted: 25 September 2026
Published: 28 September 2026

Copyright: © 2026 by the authors. Licensee MDPI, Basel, Switzerland. This article is an open access article distributed under the terms and conditions of the Creative Commons Attribution (CC BY) license.

1. Introduction

Oil recovery methods are classified as primary, secondary, and tertiary. Typically, primary and secondary oil recovery methods can recover only approximately one-third of the original oil volume due to reservoir complexities, such as heterogeneous rock pore structure, rock composition, pore and rock distribution, and reservoir fluid variability [1,2]. Tertiary recovery methods affect the rock–oil system, increasing recovery through various mechanisms. These mechanisms include reducing interfacial tension, altering reservoir wettability, reducing oil viscosity, and optimizing phase behavior [3].

For example, polymer flooding leads to an increase in the viscosity of the injected system, which leads to a decrease in the mobility coefficient and an increase in the formation coverage area [4]. Foam flooding ensures the removal of fluid from absorption zones to areas of lower permeability [5]. Alkaline solution flooding increases oil recovery due

to the microemulsification of trapped residual oil [6]. When surfactant solutions are injected, the interfacial tension of capillary-trapped oil decreases, oil viscosity decreases, and the permeability of the rock increases. These factors contribute to more efficient fluid penetration into the formation and an increase in oil production [5,7].

Recently, there has also been growing interest in the use of metal and non-metal oxide nanoparticles for enhanced oil recovery. Metal oxides (Al_2O_3, Fe_2O_3, TiO_2, and ZnO) and non-metal oxides (SiO_2) have already demonstrated significant efficiency in enhancing oil recovery due to their unique surface reactivity, stability under extreme reservoir conditions, and physical and chemical properties [8,9].

Nanoparticle-based enhanced oil recovery mechanisms have been demonstrated in numerous experiments and are widely presented in the literature. Nanoparticles migrate and pass through most of the pore channels of the reservoir via bulk flow and Brownian motion [10], and then reversibly or irreversibly are adsorbed on the surface of the formation rocks, blocking highly permeable layers and, thereby, positively adjusting the production profile [11]. It has been established that nanoparticles form wedge-shaped structures in the three-phase oil–water–solid region, causing a wedging pressure gradient. This effect, associated with the ability of one liquid to spread over a solid surface, is one of the main mechanisms of oil displacement from the rock surface [12,13]. Nanoparticles modified with hydrophilic and hydrophobic groups are adsorbed at the oil–water interface, similar to surfactant molecules, and reduce interfacial tension [14,15]. Furthermore, nanoparticles slowly settle on the rock, creating water-wetted surfaces. Thus, nanoparticles alter the wettability of the rock and positively influence the distribution of fluid flow in the reservoir [16].

Enhanced oil recovery using Al_2O_3-based nanofluids has been extensively studied in the literature [8,17,18]. Al_2O_3 nanofluids effectively reduce both the oil–mineralized water interfacial tension and oil viscosity. Experiments on oil displacement from sandstone cores showed that the best oil recovery occurred when using brine or distilled water as the dispersion medium. Additional tests on spontaneous imbibition of sandstone samples confirmed this conclusion [17]. In ref. [18], the stability of emulsions prepared with 0.05 wt.% Al_2O_3 in 3 wt.% NaCl brine and their effect on oil recovery were studied. The authors reported a reduction in interfacial tension when using alumina nanoparticles but noted that the primary mechanism for increasing oil recovery efficiency is a change in wettability. Alumina nanoparticles interact with oil-wetted mineral surfaces due to their amphoteric surface chemistry, making a change in wettability, rather than a reduction in interfacial tension, the dominant mechanism for oil recovery, especially in carbonate formations [8].

Silicon dioxide nanoparticles exhibit several mechanisms for enhancing oil recovery. Similar to aluminum oxide, silicon dioxide nanoparticles can change rock wettability from oil-wet to water-wet, effectively alter interfacial tension [19,20], and generate disjoining pressure between the discrete phase and the rock [13]. The use of hexadecylsilane-modified silica nanoparticles in salt water significantly reduces the contact angle and oil–water interfacial tension, increasing oil recovery for light oil by 25.43% [21]. In ref. [22], it was shown that for oil with a viscosity of 4.24 mPa·s, the highest oil displacement efficiency (60.6%) was observed during core flooding with a nanosuspension containing 0.25 wt.% SiO_2 nanoparticles (10 nm). In general, due to their adjustable surface properties, thermal stability, good suspension stability and the ability to simultaneously affect several extraction methods, silicon dioxide nanoparticles have great potential as additives for nanofluids in oil production operations [23].

The use of MgO nanoparticles in enhanced oil recovery applications has been studied significantly less in the literature. The effect of magnesium oxide nanoparticles on the surface tension at the oil–water interface has been studied under various conditions. An

increase in the concentration of magnesium oxide nanoparticles leads to a decrease in surface tension [24]. In ref. [25], the effect of MgO nanoparticles on changes in zeta potential, pH, and interfacial tension during electrical heating and magnetization of the nanofluid was determined. The effect of magnesium oxide nanoparticles on the zero surface charge and critical salt concentration during low-salt and alkaline flooding of formations was studied [26]. In addition, MgO is used in enhanced oil recovery applications as a rheological modifier, which optimizes interfacial tension and increases the efficiency of oil displacement [27]. In this case, the key factors influencing the use of MgO nanoparticles in enhanced oil recovery applications are particle size, size uniformity and synthesis conditions.

Common methods for synthesizing MgO nanoparticles, such as the sol–gel [28,29], coprecipitation, and hydrothermal methods [30], have significant drawbacks. These methods are characterized by poor particle size control, strong particle agglomeration, and dependence on harsh conditions or complex equipment, which limits their reproducibility and scalability [30]. An alternative and more controllable method is the synthesis of MgO nanoparticles in a polyacrylamide gel [31]. This method uses metal nitrates (e.g., $Mg(NO_3)_2$) as precursors due to their high solubility and reactivity, but these precursors pose significant risks during high-temperature calcination. Their exothermic decomposition leads to the rapid release of NOx gas, causing severe splashing, potential equipment damage, or a fire hazard. In addition, ref. [32] presents the results of a study on the effect of various chelating agents on the strength of complexation with Mg^{2+} ions using $MgSO_4$ as a precursor, the size and morphology of MgO nanoparticles, and the stability of nanosuspensions. It was found that MgO nanoparticles synthesized using hydroquinone as a chelating agent exhibit the smallest size and high colloidal stability.

The novelty of this work is defined by the material, the synthesis route, and the approach to evaluation. Unlike amphoteric SiO_2 and acidic Al_2O_3, MgO is a basic oxide whose surface basic centers interact selectively with the acidic components of crude oil. MgO also has higher thermal conductivity and thermal stability than SiO_2, yet remains much less studied in EOR, and systematic microfluidic studies of MgO nanofluids are scarce. The nanoparticles were obtained by the polyacrylamide gel method, a specialized variant of the sol–gel approach in which the crosslinked polymeric network acts as a molecular-scale nanoreactor, immobilizing the metal ions and preventing premature agglomeration. Within this route, we use hydroquinone as the chelating agent, which yields ultrafine particles and prevents the formation of stable micrometer-sized agglomerates. The study combines full nanofluid characterization with a microfluidic evaluation at five concentrations and provides quantitative data on displacement efficiency, pressure drop, and breakthrough time together with direct visualization of the displacement front.

It should be noted that the synthesis procedure itself follows the framework established in ref. [32]. The novelty of the present work lies in the application of this material to enhanced oil recovery and in the microfluidic evaluation of MgO nanofluids, which has not been reported previously. In this study, we synthesized magnesium oxide nanoparticles, prepared suspensions based on them, and conducted a microfluidic study of oil filtration in a microfluidic chip. Our results will help to better understand the mechanisms of enhanced oil recovery using MgO nanoparticles.

2. Materials and Methods

2.1. Particle Synthesis

In this work, MgO nanoparticles synthesized by the polyacrylamide gel method (see Figure 1) according to the procedure described in ref. [32] were used; however, in the present study, hydroquinone was used as a chelator. In the first step, an aqueous solution of magnesium sulfate ($MgSO_4 \cdot 7H_2O$) with a concentration of 2 mol/L was prepared. Three

separate solutions were prepared in parallel: acrylamide (monomer), MBAA (crosslinking reagent), and ammonium persulfate (polymerization initiator). The metal salt solution was combined with the monomer in a three-necked flask equipped with a stirrer, thermometer, and condenser. After a homoegeneous mixture was achieved, the pH was adjusted to 9 using KOH or HCl. Then, the initiator and crosslinking agent were sequentially introduced into the reaction system in quantities of 0.3 and 5 wt.%, respectively (relative to the monomer). The reaction mixture was heated to 80 °C and maintained at this temperature until a three-dimensional polymer network was formed in which magnesium cations were immobilized.

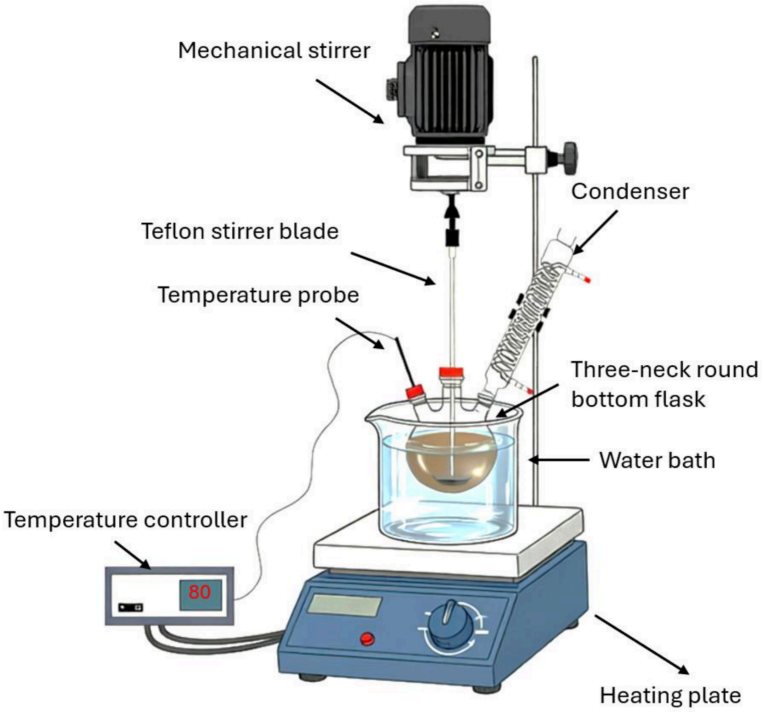


Figure 1. Scheme of synthesis of MgO nanoparticles by the polyacrylamide gel method.

The formed hydrogel was separated from the flask walls and transferred to a vacuum oven for drying at 80 °C (duration: two days). Complete removal of moisture yielded a hard, brittle material (xerogel). The xerogel was mechanically ground in an agate mortar, after which the resulting powder was placed in a corundum crucible. Heat treatment was performed in a muffle furnace in air: the sample was heated to 800 °C at a rate of 5 °C/min, held at this temperature for two hours, and then cooled to room temperature without forced rate control. During calcination, the polymer component burned off and the magnesium sulfate decomposed, resulting in the formation of magnesium oxide as a white nanosized powder.

The key difference between the presented method and the reference protocol [32] is the use of hydroquinone as a complexing additive during the preparation of the precursor solution. All quantitative synthesis parameters (reagent concentrations, temperature and time regimes, and pH) fully correspond to the reference conditions adopted in the original work. In ref. [32], the chelating agents investigated were EDTA and citric acid, whereas hydroquinone was not examined. Its use here is therefore a deliberate extension of that work rather than a reproduction of the reference protocol. The resulting MgO powder was subjected to a range of physicochemical analytical methods without any additional purification, which fully reproduces the characterization scheme proposed in ref. [32]. This approach ensures comparability of results and allows us to identify the effect of chelator replacement on the structural and morphological characteristics of the final product.

2.2. Preparation of Nanofluids

Nanofluids were prepared using an FB15051 ultrasonic bath (Fisher Scientific, Waltham, MA, USA) with a power of 280 W. MgO powder was dispersed in distilled water to obtain suspensions. To achieve a reproducible dispersed state, an optimized pulse protocol was used, including two 30 s ultrasonic treatments with a 15 min break between cycles. The choice of this mode was justified by the results of preliminary optimization carried out for a reference sample synthesized according to the protocol (6 min treatment without breaks) [32]. Visual monitoring of the dispersion state was performed after each cycle until a homogeneous suspension without visible sediment was achieved.

2.3. Acoustic Spectroscopy and Electron Microscopy

Particle size and distribution in the suspension were determined using acoustic spectroscopy on a DT 1202 instrument (Dispersion Technology Inc., Bedford Hills, NY, USA). This method measures the attenuation of acoustic waves in a suspension and allows particle size distributions over a wide range to be obtained without pre-diluting the samples. Measurements were performed at room temperature in triplicate using a 1 wt.% suspension prepared according to a standard procedure.

Particle morphology was examined using scanning electron microscopy (SEM) on an SU3500 microscope (Hitachi, Tokyo, Japan). SEM was performed at an accelerating voltage of 5 kV, a working distance of 8.3 mm, and a magnification of $\times$30,000 using a secondary electron (SE) detector.

The elemental composition of the synthesized powder was determined by X-ray fluorescence (XRF) spectroscopy on a PANalytical Axios-MAX wavelength-dispersive spectrometer (PANalytical, Almelo, The Netherlands). The analysis provided the mass fractions of magnesium and sulfur in the final product. The instrument does not detect light elements such as oxygen and carbon, so the reported values were used as a comparative measure of relative magnesium enrichment and residual sulfur after calcination, without recalculation to oxide equivalents.

2.4. Colloidal Stability Measurement

The colloidal stability of MgO nanoparticle suspensions was assessed using a Multiscan MS-20 multibeam scanning dispersion stability analyzer (DataPhysics Instruments GmbH, Filderstadt, Germany). The instrument is equipped with a pulsed near-infrared light source (880 nm) and two synchronously moving photodetectors that simultaneously record the intensity of transmitted and backscattered radiation across the entire height of a glass cuvette (scan height 55 mm, step 0.1 mm). This approach allows for the detection of changes in particle concentration in different zones of the sample at the early stages of destabilization without external perturbation of the system. Measurements were performed at room temperature for 4 h with automatic profile recording at specified time intervals. The resulting transmission profiles were used to assess sedimentation stability and draw conclusions about the behavior of the dispersed system over time.

2.5. Viscosity Measurement

A DVNext rotational viscometer (DVNext Inc., Bedford, MA, USA) was used in conjunction with a CPZ-40 measuring cone, which provides high measurement accuracy over a wide range of shear rates (Figure 2). The measurement process included the sequential determination of viscosity at different shear rates in the range of 250 to 1875 s^{-1}. The measurement technique involved placing the sample in the viscometer's measuring cell with the CPZ-40 cone installed, setting the required thermostatting temperature, and holding the sample until temperature equilibrium was reached. Subsequently, sequential viscosity

measurements were performed at different shear rates. For each sample, at least three repeated measurements were taken to determine the average value and estimate the error. All measurements were conducted at a constant temperature of 25 °C.

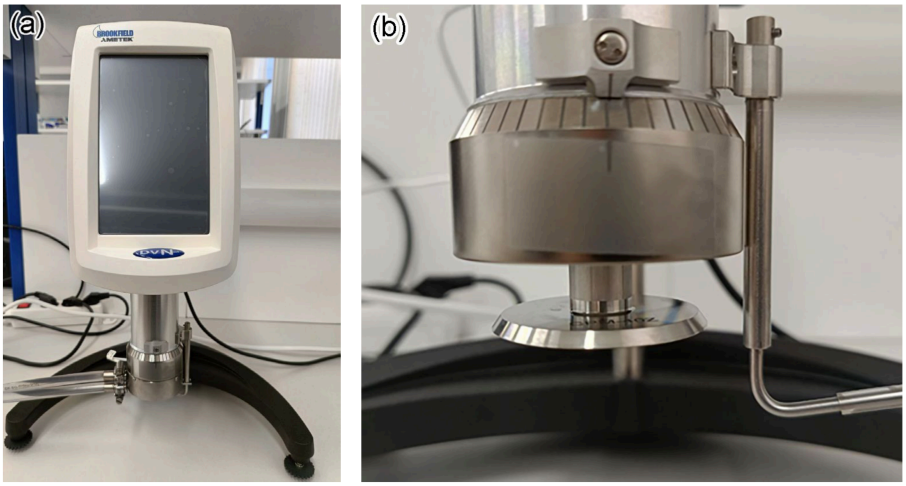


Figure 2. Rotational viscometer (**a**) and measuring cone (**b**).

2.6. Surface Tension

The surface tension of the resulting suspensions was measured using a K6 manual tensiometer (Krüss, Hamburg, Germany) by the ring pull-off method (Figure 3). Before measurements, the platinum–iridium ring was thoroughly cleaned by heating it in a gas burner flame. Measurements were performed at room temperature (25 ± 1 °C). At least five consecutive ring pull-offs were recorded for each suspension. The final surface tension value was calculated as the arithmetic mean of all measurements. The standard deviation did not exceed 0.5 mN/m, indicating good reproducibility of the results.

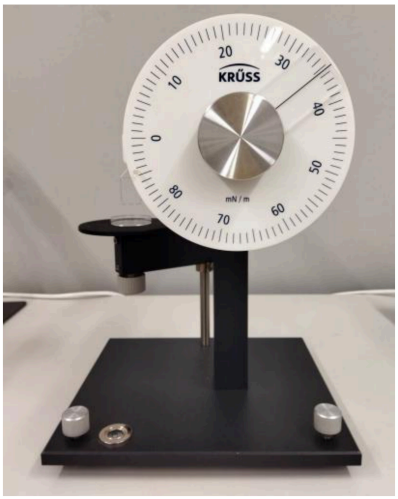


Figure 3. Manual tensiometer K6.

2.7. Microfluidic Filtration

The oil used in the microfluidic experiments had a density of 874 kg/m^3 and a viscosity of 47 mPa·s at 25 °C. The displacing phase was an aqueous MgO suspension prepared at concentrations of 0.25 wt.% and 2 wt.% in distilled water. The chip was first saturated with oil, after which the MgO suspension was injected at a constant flow rate of 0.1 µL/min. All experiments were performed at room temperature (25 °C) and atmospheric pressure. Each experiment was repeated three times, and the reported values are averages of the three

replicates. The relative error in the determination of the displacement efficiency did not exceed 1%.

Microfluidic experiments were performed using the setup schematically shown in Figure 4a. A detailed description is provided below. A microfluidic chip model of the porous medium of a terrigenous reservoir (see Figure 4b) was used. The model was generated using cylinders with sizes ranging from 18.6 to 237.6 μm. The pore volume was 0.837 μL, and the width and length of the porous region were 3752 and 8682 μm, respectively. The channel depth of the entire micromodel was 40 μm.

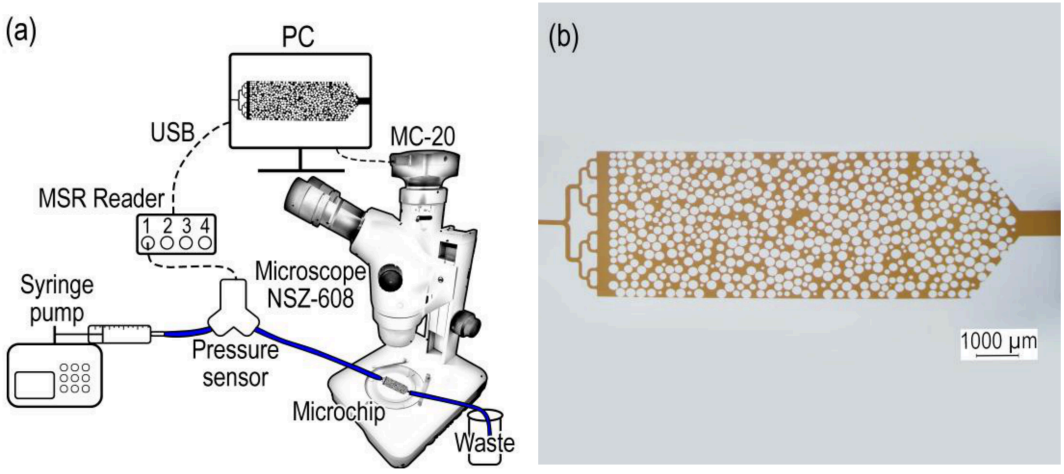


Figure 4. Schematic diagram of the experimental setup (**a**) and a photograph of the microfluidic chip filled with oil (**b**).

Fluid was supplied using an SPlab01 syringe pump (Shenchen, Baoding, China). Flow rates ranged from 0.831 nL/min to 127 mL/min, with a flow rate accuracy of ±0.5%. The syringe (Hamilton, Bonaduz, Switzerland) had a capacity of 500 μL and a Luer-TLL (Luer Tip) connection. A 1/16" OD PTFE tube was used to connect the microfluidic chip, pressure sensor, and syringe pump, as shown in Figure 4a. The chip was mounted horizontally on the slide of an NSZ-608 stereoscopic microscope (Nanjing Jiangnan Novel Optics Co., Ltd., Nanjing, China). Data were recorded using an MC-20 digital camera microscope (Microanaliz LLC, St. Petersburg, Russia). Subsequently, the resulting video files were converted into images using FFmpeg, version 7.1. The system pressure was monitored using an MPS 3 sensor (Elveflow BV, Amsterdam, The Netherlands). The MSR Read module was used to record data from the pressure sensor. The pressure sensor operating range was −1000 to 2000 mbar. The error was not more than ±0.2% of the maximum pressure, and the repeatability was ±0.2%.

To analyze the oil displacement coefficient, the "Program for analyzing water and oil saturation in a porous structure (Oil Recovery Image Analyzer)" was used. This program allows for the automatic determination of the oil displacement coefficient by processing and threshold segmentation of experimental images of models in a selected area of the image.

The primary silicon master mold was fabricated using photolithography and reactive ion etching. To prevent adhesion between silicon and PDMS, the master mold was vacuum-treated with trichloro (1H,1H,2H,2H-perfluorooctyl) silane vapor for 24 h. After silanization, a primary print was obtained from the silicon master mold using PDMS (Sylgard 184, Dow Corning) according to the manufacturer's instructions. The PDMS master mold was then used to create the final microfluidic chips using KER 215 epoxy resin and KCA4303 curing agent (Kumho Petrochemical Group) [33] (see Figure 5). New chips were created for each experiment to ensure that the initial experimental conditions were always the same.

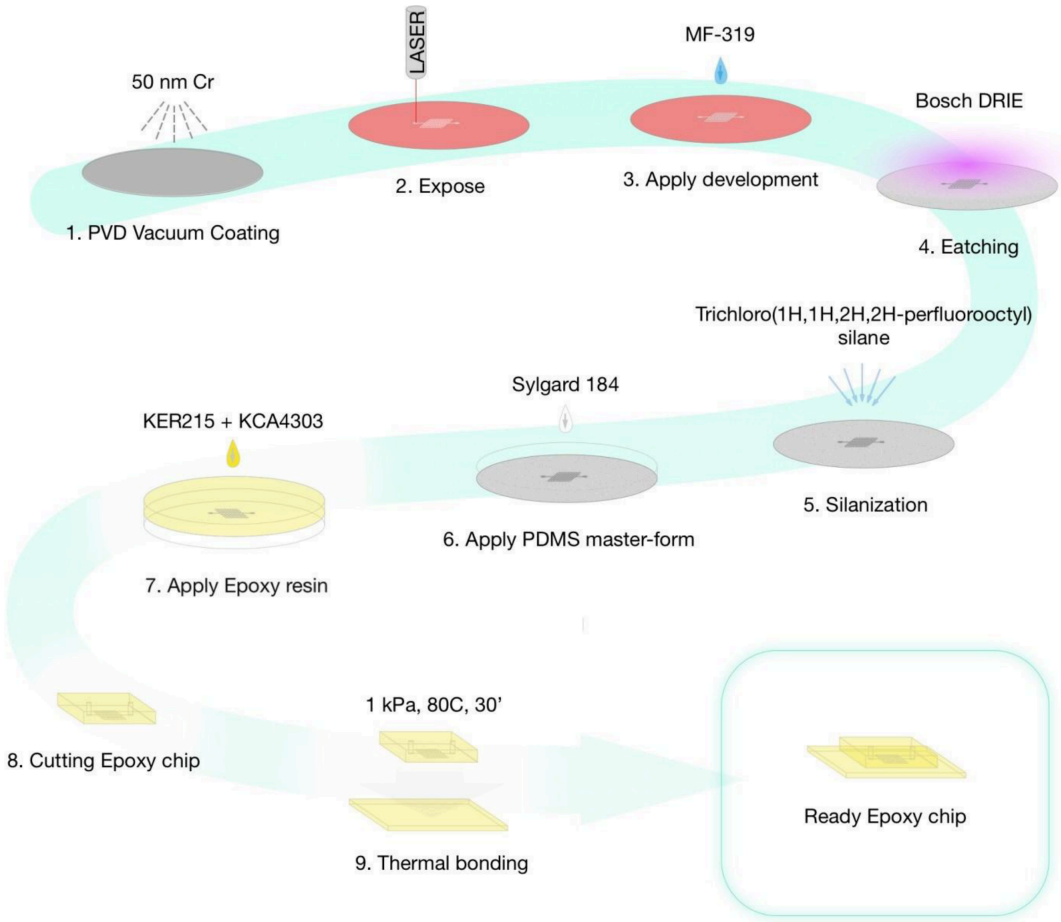


Figure 5. Basic diagram for making a master mold and chips from epoxy resin.

The epoxy micromodel reproduces the topology of the pore network but not the absolute pore size or the surface chemistry of a natural rock. The results are therefore presented as a mechanistic and comparative study rather than a direct quantitative prediction of field-scale recovery.

3. Results and Discussion

3.1. Optimization of Ultrasonic Treatment of Suspensions

This subsection is devoted to the systematic optimization of the process for obtaining a monodisperse and stable suspension for microfluidic analysis and oil displacement rate assessment. The optimization was conducted to determine the minimum ultrasonic treatment time required to form a homogeneous colloidal system.

At the initial stage of the work, the standard protocol used in ref. [32] for reference samples (6 min ultrasonic treatment at 280 W without breaks) was adopted for the preparation of the nanofluid. An alternative optimized protocol included the use of ultrasonic treatment with two short 30 s pulses and a 15 min break between cycles. The effectiveness of the protocols was quantitatively assessed using acoustic spectroscopy. Figure 6 shows a comparison of the particle size distribution of the MgO sample treated in the standard ultrasonic treatment mode and with the optimized pulse method.

An analysis of the distribution after the standard protocol (Figure 6a) shows that continuous six-minute processing results in a bimodal distribution. The first mode is characterized by an average size of ~80 nm, while the second mode corresponds to particles in the micron range with a maximum at 6.1 μm. The micron fraction accounts for 24%, and the standard deviation of the distribution is 0.2. The smaller size of the primary

mode compared to the optimized protocol (~80 nm versus ~95 nm) indicates a more intense fragmentation of agglomerates under prolonged ultrasonic treatment. However, the appearance of a pronounced secondary peak in the micrometer range indicates the reverse process (intense re-agglomeration) caused by excessive energy exposure. Thus, the continuous protocol, despite its effective fragmentation, leads to a deterioration of colloidal homogeneity and the formation of large, stable agglomerates.

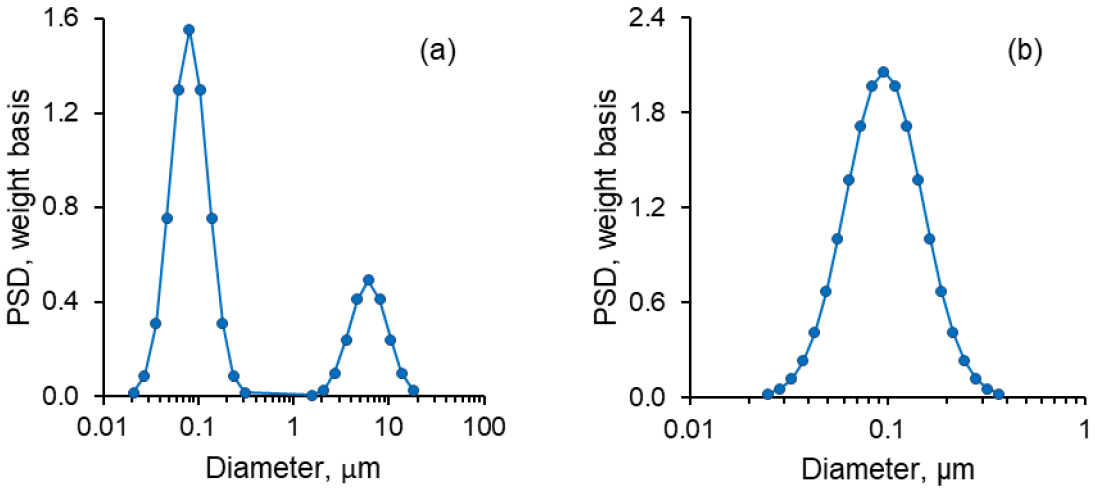


Figure 6. Particle size distribution of a reference sample of MgO nanoparticles after standard sonication (**a**) and optimized pulsed sonication (**b**).

With the optimized pulsed protocol (Figure 6b), the particle distribution becomes unimodal. The second micrometer mode is completely absent; the average size of the single population is ~95 nm, and the standard deviation decreases to 0.19. The elimination of the secondary peak in the micrometer range indicates the effective destruction of large agglomerates, and the slight increase in the average size of the primary mode is explained by the removal of small fragments that formed micrometer-sized clusters in the standard protocol. The absence of particles in the micrometer range is a key advantage of the pulsed mode, ensuring the production of a homogeneous colloidal system.

Thus, the optimized pulse protocol allows for the production of a monodisperse suspension with reproducible physicochemical properties, which is critical for accurately assessing oil displacement efficiency in microfluidic experiments. This protocol was used to prepare all suspensions studied in this study.

3.2. Characterization of Particles and Suspensions

Figure 7a shows an SEM micrograph of the synthesized MgO nanoparticles. The particles have a predominantly isometric, nearly spherical morphology with distinct edges characteristic of the periclase crystal structure. The size of the observed objects ranges from 230 to 480 nm. However, it should be noted that the SEM image captures the structure of a dried droplet, in which the primary nanoparticles form dense agglomerates under the action of capillary forces during solvent removal.

Acoustic spectroscopy results (Figure 7b) show that the particle distribution in the liquid suspension is bimodal. The primary mode is characterized by an average size of 14 nm, while a secondary, minor mode (9%) corresponds to particles with a size of approximately 77 nm. The standard deviation is the same for both modes and is 0.33, indicating a moderate peak width and sufficient particle homogeneity within each fraction. The absence of a population in the micrometer range confirms that the synthesized nanoparticles do not form irreversible microagglomerates in the suspension, and ultrasonic treatment ensures effective disaggregation.

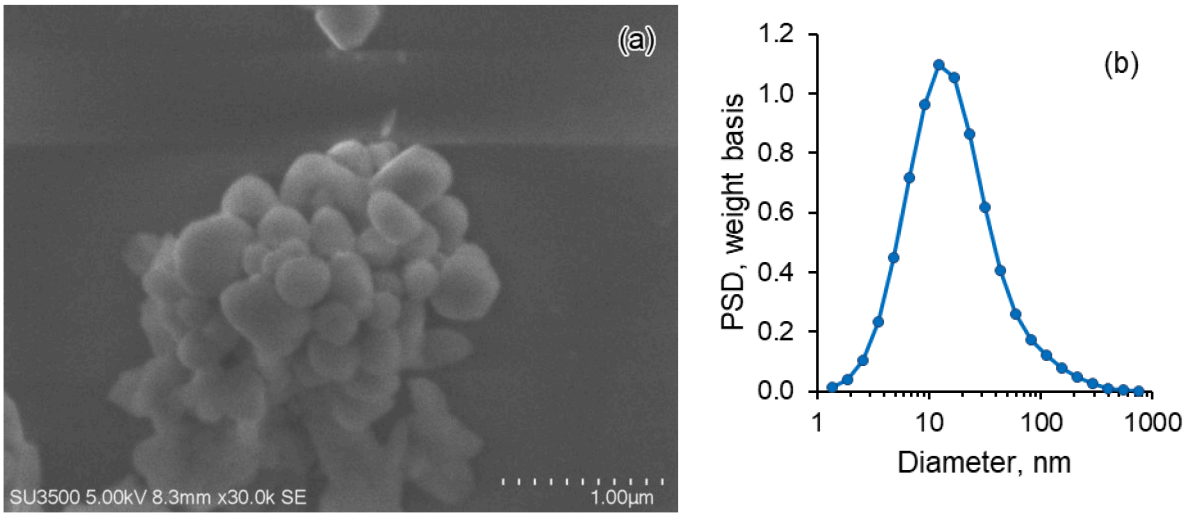


Figure 7. SEM micrographs (**a**) and size distribution of MgO nanoparticles (**b**) synthesized with hydroquinone as a chelating agent.

The difference in sizes recorded by SEM and acoustic spectroscopy is due to fundamental differences in the methods. Electron microscopy visualizes dry agglomerates on a substrate, while acoustic spectroscopy measures the hydrodynamic diameter of disaggregated particles directly in the liquid phase. Both methods complement each other and, together, provide a complete picture of the dimensional characteristics of the synthesized material.

The difference between the two values reflects what each method measures. SEM shows dried particles under vacuum. During drying, the primary particles stick together into agglomerates, so the SEM images show agglomerates of 230–480 nm. Acoustic spectroscopy measures the particles in the liquid, without drying or dilution, and gives a bimodal distribution with a main mode at 14 nm and a minor mode at 77 nm. The larger SEM value therefore corresponds to the dried agglomerates, and the smaller acoustic value corresponds to the particles in the suspension. This is consistent with the colloidal stability data, which show no sedimentation and no micrometer-sized particles.

Thus, the use of hydroquinone as a chelating agent in the synthesis of MgO nanoparticles allows production of particles with a size of 14 nm. A small second mode at 77 nm (9%) likely corresponds to stable dimers or small aggregates of primary crystallites. The differential distribution curve (Figure 7b) does not reveal particles in the micrometer range, indicating effective disaggregation under the suspension preparation conditions and allowing the resulting material to be considered promising for further rheological and microfluidic studies. To confirm the chemical identity and phase purity of the final product, the powder was additionally characterized by XRF.

The XRF analysis of the final powder yields 89.38% Mg and 8.40% S, normalized to the sum of the detected elements, with 2.21% K. The high relative magnesium content and the low residual sulfur confirm that the sulfate precursor decomposed almost completely during calcination and that the final product is predominantly magnesium oxide. Since XRF does not detect oxygen, these values serve as a comparative measure of magnesium enrichment and residual sulfur rather than an absolute MgO content.

3.3. Colloidal Stability

To assess the stability of the synthesized MgO suspensions, a multibeam scanning method was used, allowing for real-time recording of changes in light transmittance along the sample's height. Figure 8 shows the transmittance profiles for the four studied concentrations after 4 h of observation.

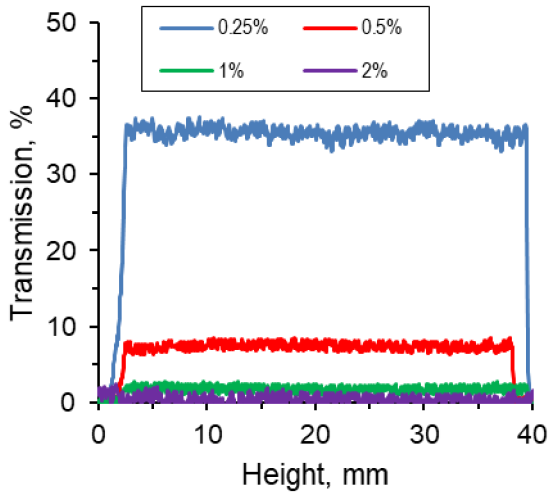


Figure 8. Transmission profiles in the considered suspensions with different concentrations of nanoparticles.

In all cases, the transmittance profiles remained virtually unchanged throughout the experiment, indicating the absence of significant sedimentation or aggregation of particles. The average transmittance value decreases consistently with increasing nanoparticle concentration, from 35.5% for the most dilute suspension (0.25 wt.%) to 0.38% for the highest concentration (2 wt.%). This decrease is due to an increase in the volume fraction of the solid phase and a corresponding increase in light scattering, which is characteristic of stable colloidal systems with high optical density. The absence of a transmittance gradient along the height of the cuvette indicates a uniform distribution of particles throughout the sample, without the formation of a precipitate or a distinct clear zone at the top of the suspension.

The obtained data confirm the high sedimentation stability of the studied nanofluids for a time sufficient to conduct microfluidic experiments.

3.4. Rheological Properties

The viscosity measurements of the suspensions, as well as the effect of MgO nanoparticle concentration on their viscosity, are presented in Figure 9. An analysis of the shear stress versus shear rate (Figure 9a) shows that all the studied MgO nanofluids exhibit Newtonian behavior. Shear stress increases linearly with increasing shear rate, while viscosity remains constant over the entire range of shear rates studied.

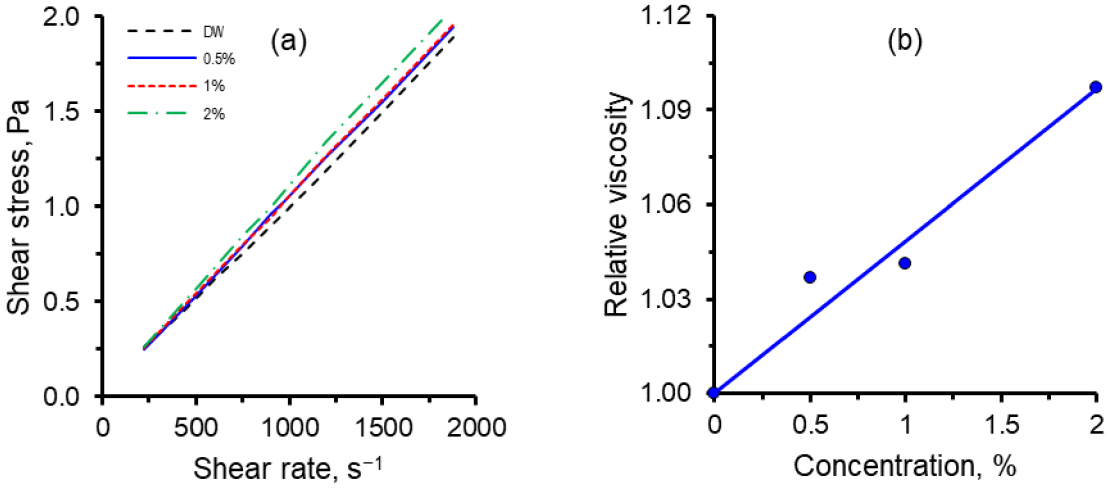


Figure 9. Dependence of shear stress on shear rate (**a**) and viscosity on concentration (**b**) of MgO nanoparticles in suspension.

The effect of nanoparticle concentration on the relative viscosity of suspensions is shown in Figure 9b. As can be seen from the data presented, the introduction of MgO nanoparticles leads to a slight increase in viscosity. Thus, with an increase in particle mass concentration to 2%, the relative viscosity increases to 1.097, corresponding to an increase of less than 10% relative to water. Moreover, over the studied concentration range, a roughly linear relationship between relative viscosity and nanoparticle content is observed.

It is important to note that the experimentally obtained viscosity values significantly exceed those predicted by the classical Einstein theory for spherical particles. According to the Einstein theory, for a volume fraction of the solid phase corresponding to 2 wt.% MgO (taking into account the density of MgO as ~3.58 g/cm^3, the volume fraction φ is ≈0.565 vol.%), the relative viscosity should be $\eta_{rel} = 1 + 2.5\varphi \approx 1.014$. The experimental increase in viscosity is almost 7 times greater than the theoretical value. This excess is a characteristic feature of nanofluids and is due to nanoscale effects that are not taken into account by Einstein's model. This fact fundamentally distinguishes the behavior of nanosuspensions from classical colloidal systems with micron particles and confirms the high quality of synthesis, ensuring the preservation of the nanoscale properties of the particles.

The obtained rheological data indicate that MgO nanofluids maintain Newtonian behavior up to the maximum concentration studied, and the controlled increase in viscosity with increasing particle content is favorable for use in oil displacement technologies. A predictable increase in suspension viscosity improves the mobility ratio of the injected fluid to the reservoir oil. This contributes to an increase in formation sweep efficiency during displacement and prevents the formation of viscous fingers. However, a minor increase in viscosity cannot be the sole primary mechanism for enhancing oil displacement.

3.5. Surface Properties

Analysis of surface properties revealed that the surface tension of the suspensions at the interface with air remained virtually unchanged across the entire studied concentration range and was 72–73 mN/m, which corresponds to the value for distilled water. This clearly demonstrates the absence of surface-active properties in the synthesized MgO nanoparticles. Direct measurement of the interfacial tension at the interface with oil using optical tensiometry was impossible due to the opacity of the suspensions. However, given that the particles showed no activity at the interface with air, it can be concluded that their effect on the interface with oil is also negligible.

3.6. Results of the Microfluidic Experiment

The effectiveness of nanoparticles in displacing residual oil depends largely on their concentration in the injected fluid. The optimal concentration should be sufficient to significantly alter interfacial forces and wettability but not so high as to clog pore channels, damage the formation, or become economically unviable.

Figure 10 shows photographs of the displacement process for MgO-0.25% and MgO-2% in comparison. The volumetric displacement flow rate was 0.1 μL/min. The displacement dynamics for MgO-0.25% are similar to the displacement process when pumping distilled water [34]. At the beginning (the first 30 s), a uniform distribution of the displacing fluid throughout the pore space is observed. The front then splits into separate streams and moves approximately to the middle of the chip along the lower part of the channels (2 min of displacement). Then, the liquid moves along the upper part and reaches the exit of the microchip (5 min of displacement). After the displacing liquid has exited, the flow stabilizes and proceeds along the formed channels (20 min of displacement). The entire displacement process for MgO-0.25% took approximately 184 s; compared to water, this is three seconds

longer. For MgO-2%, the dynamics of the displacement process at the beginning (first minute) are similar to the displacement for MgO-0.25%. Clear differences in displacement for MgO-2% begin in the second minute. The displacement front forms a wedge shape; the process involves filling the upper region in the first half of the chip, and displacement also proceeds along the upper region of the pore space of the chip and reaches the exit of the chip (5 min for MgO-2%). The entire displacement process for MgO-2% took approximately 257 s, which is 74 s longer than that for MgO-0.25%.

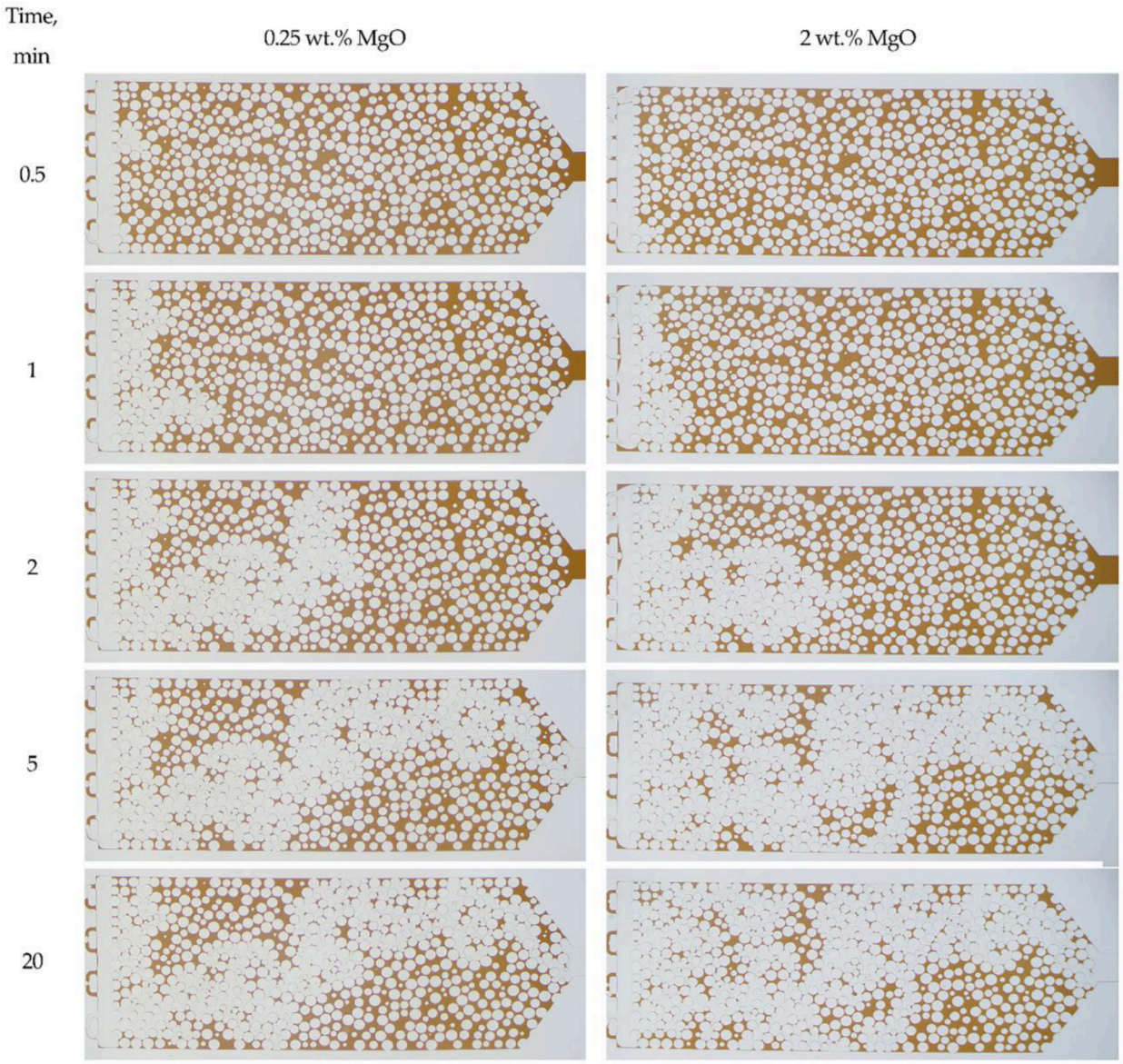


Figure 10. Photographs of the oil and suspension distribution inside the microfluidic chip during the displacement process for the 0.25 wt% and 2 wt% MgO suspensions at different time points.

Experiments were conducted to study the effect of MgO concentration, as shown in Figure 11. The final displacement photographs for the first three concentrations are very close to those of water, but for the maximum concentration, the final displacement differs from the others. The displacement efficiency (K_{disp}) for pure distilled water was 44.15%. It was found that with increasing concentration, an increase in displacement efficiency is observed. Thus, for the MgO nanofluid with a mass concentration of 0.25%, the K_{disp} was 44.28%, which is 0.13% higher than that of water. Increasing the MgO concentration to 0.5 wt.% yields a K_{disp} of 47.05%, representing an increase of 2.77% relative to the

previous concentration and 2.9% relative to distilled water. A further increase in the MgO concentration to 1 wt.% results in an increase in K_{disp} by 0.44% compared to a concentration of 0.5%, and in comparison with water, K_{disp} increases by 3.21%. The maximum effect of K_{disp} is achieved at a concentration of 2 wt.%, and amounts to 54.98%, which is 7.49% higher than at 1 wt.%, and in comparison with pure water, it results in an increase in K_{disp} by 10.83%.

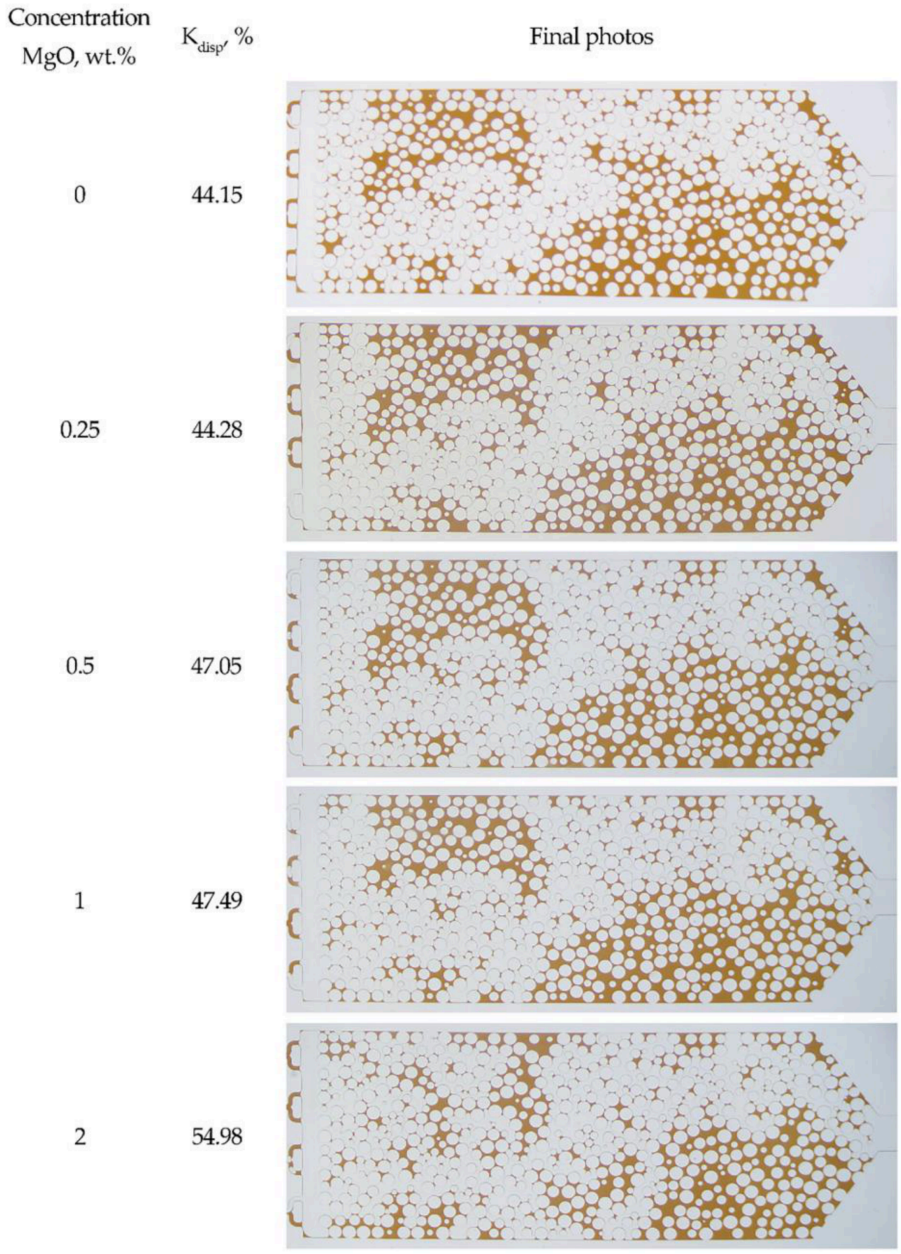


Figure 11. Final photographs of oil-displacing fluids based on MgO nanosuspensions depending on concentration.

The dependence of the displacement efficiency and pressure drop on time in Figure 12 is noteworthy. The displacement dynamics in the graph in Figure 12a have the same slope for all samples during the first 3 min, indicating that the displacement process was stable for all samples. After displacement, the graph shows how the flow in the channels stabilized and followed the formed channels. The change in pressure drop over time is shown in Figure 12b. The flow rate remained constant at 0.1 μL/min in all displacement experiments, so any changes in the measured pressure reflect changes in the hydraulic

resistance of the porous medium rather than changes in the imposed flow rate. The measured pressure represents the total pressure drop across the chip and comprises a hydrodynamic component associated with viscous flow through the pore network and a capillary component associated with the menisci at the fluid interfaces. These components behave differently during displacement, which explains the shape of the pressure curve in Figure 12b.

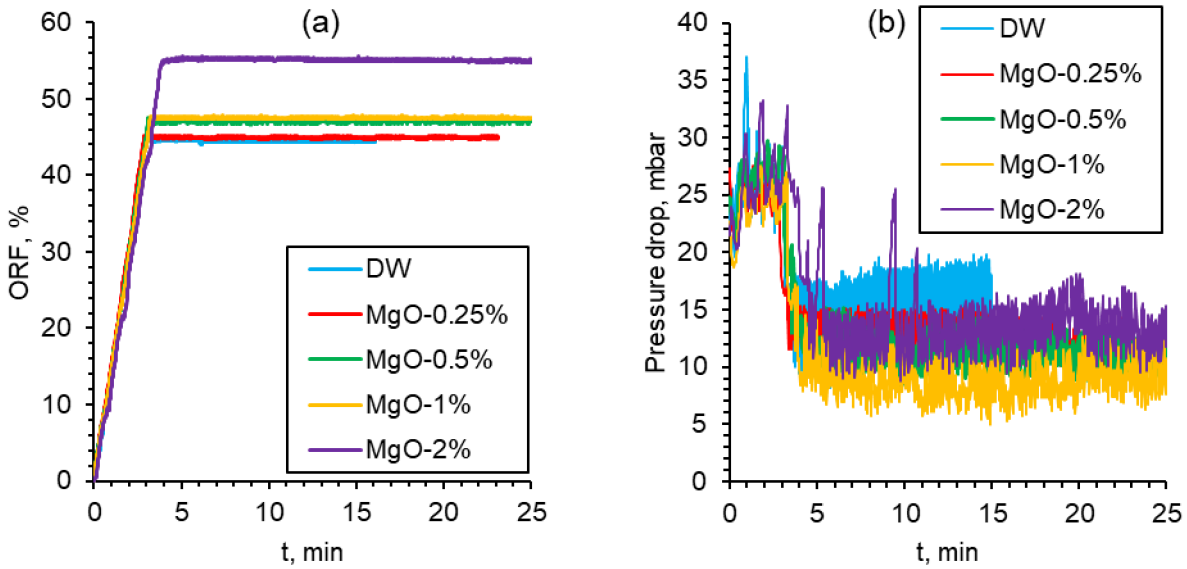


Figure 12. Graph of displacement efficiency (**a**) and pressure drop (**b**) versus time.

At the beginning of the experiment, the nanofluid enters the pore space and displaces the oil initially present in the pore network and inlet channels. At this stage, the displacing fluid must overcome the capillary resistance of the oil-filled pores and establish a continuous flow path, while the effective cross-section available for flow is still limited. Both effects increase the total hydraulic resistance, and over the first ~3 min the pressure rises.

Once the fluids begin to exit the pore space of the chip and a connected path is established through the porous zone, the capillary resistance gradually decreases as the oil is mobilized and the wettability of the pore walls changes. This is reflected in the smooth decline of the pressure, clearly visible in Figure 12b over the time interval corresponding to the displacement process (K_{disp}), and in the change in the pressure drop. In the subsequent portion of the curve, the pressure reaches a plateau, which corresponds to a steady-state flow regime in which the displacing agent flows through the already formed channels with no further oil recovery. At this stage, the hydrodynamic component dominates and the capillary component becomes essentially constant, so the total pressure drop stabilizes.

The summarized results of the displacement experiments for all studied oil-displacing fluids are shown in Figure 13. As described above, the plot of the displacement efficiency versus nanofluid concentration shows an increase in K_{disp} with increasing MgO mass concentration (see Figure 13a). A different picture is observed in the pressure drop plot. With increasing concentration, the average pressure drop for pumping the nanofluid decreases and reaches a minimum of 11.20 mbar at 1 wt.%. A further increase in concentration to 2 wt.% increases the average pressure drop to 15.71 mbar, which is 4.51 mbar higher than that for MgO-1% but still lower than the average pressure drop for water (see Figure 13b). The plot of the displacing fluid breakthrough time versus concentration shows a trend similar to that of the displacement efficiency. For water and MgO-0.25 wt.%, the breakthrough times are virtually identical, differing by only a few seconds. A significant difference in breakthrough time begins at a concentration of 0.5% and increases with further increasing

concentration. The maximum breakthrough time is observed for the MgO-2 wt.% nanofluid, amounting to 4.28 min (see Figure 13c).

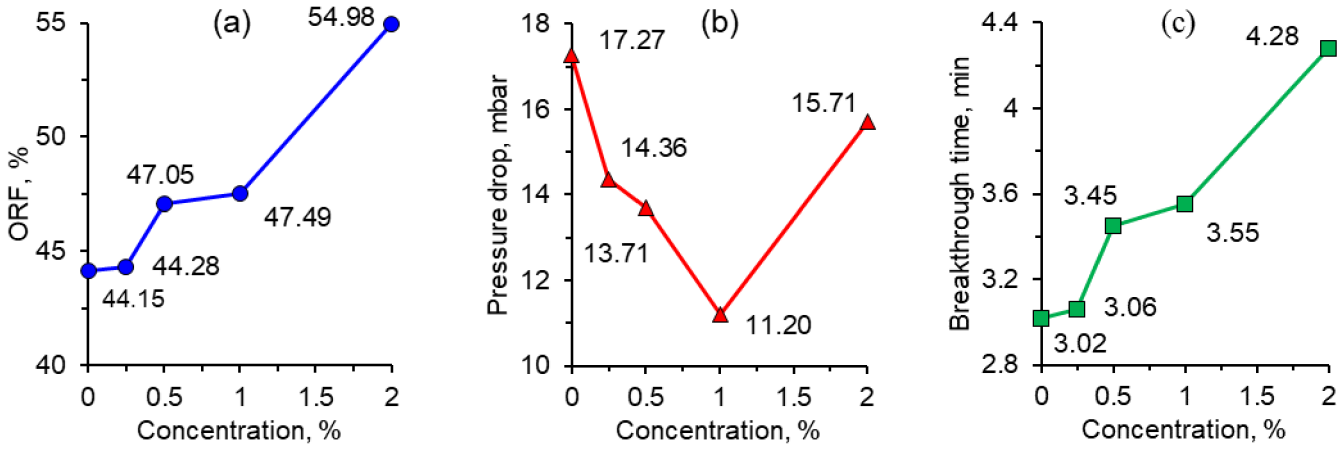


Figure 13. Graphs of quantitative indicators of oil-displacing fluids depending on the concentration of MgO nanoparticles: displacement coefficient (**a**), pressure drop (**b**), and breakthrough time (**c**).

It is useful to compare these results with those for the SiO_2 and Al_2O_3 nanofluids studied previously on the same microfluidic setup and with the same oil and flow rate [35]. At 0.5 wt.%, the displacement efficiency was 46.26% for 10 nm SiO_2, 44.32% for 45 nm SiO_2, and 45.43% for Al_2O_3 nanofibers, compared with 44.15% for water. The MgO nanofluid used here yields 47.05% at the same concentration, which is higher than all three oxide systems. Data at higher concentrations are not available for SiO_2 and Al_2O_3, so the comparison is made at equal particle concentration. This shows that MgO is at least as effective as, and in this case slightly more effective than, the oxide systems tested, and that its advantage becomes more pronounced at higher concentration while the suspension remains colloidally stable.

Thus, the obtained results demonstrate a direct positive relationship between the concentration of MgO nanoparticles in the suspension and oil displacement efficiency, pressure drop, and breakthrough time. Among the five concentrations studied, 2 wt.% was the most effective. It should be noted that the optimal concentration is not universal and depends on pore-throat size distribution, permeability, salinity, and particle surface chemistry, so 2 wt.% should be understood as the optimum for the specific MgO nanofluid, oil, and micromodel used here.

The data from the microfluidic experiments conducted at various nanofluid concentrations allow us to summarize the observed trends and quantify the impact of MgO nanoparticle content on oil displacement efficiency.

4. Conclusions

Microfluidic experimental studies of oil-displacing fluids based on magnesium oxide nanoparticles synthesized in the presence of hydroquinone as a chelating agent were conducted. The efficiency of oil displacement from model microchips by nanofluids with varying concentrations of MgO nanoparticles was assessed. The stability and rheological properties of the studied nanofluids were determined, as well as the dependence of the oil displacement efficiency and pressure drop during flooding of the microchips with the studied solutions. The front movement pattern during oil displacement was analyzed. The synthesis followed the polyacrylamide gel route established in ref. [32], with hydroquinone introduced here as the chelating agent. The contribution of this work is the microfluidic evaluation of the resulting MgO nanofluids for enhanced oil recovery.

The synthesis of MgO nanoparticles using hydroquinone as a chelating agent yielded particles measuring 14 nm. Importantly, the suspension was completely free of micrometer-sized agglomerates. Acoustic spectroscopy did not detect particles larger than 100 nm, indicating effective disaggregation and high colloidal stability. Thus, hydroquinone acted not simply as a chelator but also as a structure-directing agent, ensuring the formation of ultrafine particles with a narrow size distribution.

All studied MgO nanofluids exhibited colloidal stability, which is necessary for reproducible rheological measurements and accurate interpretation of microfluidic displacement results.

Rheological measurements showed that all studied suspensions behaved like Newtonian fluids. Viscosity was independent of shear rate and increased linearly with particle concentration, increasing to 1.096 mPa·s as the MgO content reached 2 wt.%.

Microfluidic experiments on model chips confirmed the efficiency of MgO suspensions for oil displacement. With water flooding, the displacement efficiency was 44%. The addition of 0.5 wt.% particles increased it to 47%, and with 2 wt.%, the efficiency reached 55%, which is 10.8% higher than that of water. At equal concentration, the MgO nanofluid yielded a higher displacement efficiency than the SiO_2 and Al_2O_3 nanofluids tested under identical conditions.

Moreover, the surface tension of the suspensions remained at the level of pure water (72–73 mN/m), which excludes the capillary mechanism. Consequently, the observed effect is associated with an increase in the viscosity of the displacing agent and, likely, a change in the wettability of the rock due to the adsorption of nanoparticles on the surface and the formation of disjoining pressure in thin wetting films. The obtained results are consistent with the mechanism described in ref. [36] and open up prospects for the use of synthesized MgO suspensions in enhanced oil recovery technologies. Among the concentrations studied, 2 wt% gave the highest displacement efficiency, and this value should be understood as the most effective concentration for the specific system used here.

Author Contributions: Conceptualization, A.M. and H.B.A.; methodology, M.P., H.B.A. and A.M.; formal analysis, M.P., H.B.A. and A.P.; investigation, M.P., H.B.A., S.K., R.V., V.Z. and A.P.; resources, A.M.; data curation, A.M.; writing—original draft preparation, M.P., H.B.A., V.Z., A.P. and A.M.; writing—review and editing, M.P., H.B.A., V.Z., A.P. and A.M.; visualization, M.P., H.B.A., S.K., R.V. and A.P.; supervision, A.M.; project administration, A.M.; funding acquisition, A.M. All authors have read and agreed to the published version of the manuscript.

Funding: The research was supported by grant no. 23-79-30022 of the Russian Science Foundation, https://rscf.ru/project/23-79-30022/ (accessed on 14 August 2026).

Data Availability Statement: The original contributions presented in this study are included in the article. Further inquiries can be directed to the corresponding authors.

Conflicts of Interest: The authors declare no conflicts of interest.

References

1. Jafarbeigi, E.; Zarei, H.; Mansouri, M.; Kikhavani, T.; Setareshenas, N. Investigating a new synergistic nanofluid to improve oil recovery mechanisms in oil reservoirs. *J. Mol. Liq.* **2025**, *439*, 128827. [CrossRef]
2. Muggeridge, A.; Cockin, A.; Webb, K.; Frampton, H.; Collins, I.; Moulds, T.; Salino, P. Recovery rates, enhanced oil recovery and technological limits. *Philos. Trans. A Math. Phys. Eng. Sci.* **2014**, *372*, 20120320. [CrossRef]
3. Alvarado, V.; Manrique, E. Enhanced Oil Recovery: An Update Review. *Energies* **2010**, *3*, 1529–1575. [CrossRef]
4. Zhang, J.; Wang, X.; Liang, Q.; Duan, M.; Fang, S.; Zhang, C.; Chen, J. Demulsification law of polyether demulsifier for W/O crude oil emulsion containing hydrophobically modified polyacrylamide in water. *J. Mol. Liq.* **2024**, *394*, 123805. [CrossRef]
5. Huang, S.; Jiang, G.; Guo, C.; Feng, Q.; Yang, J.; Dong, T.; He, Y.; Yang, L. Experimental study of adsorption/desorption and enhanced recovery of shale oil and gas by zwitterionic surfactants. *Chem. Eng. J.* **2024**, *487*, 150628. [CrossRef]

6. Sarbast, R.; Salih, N.; Préat, A. A Critical Overview of ASP and Future Perspectives of NASP in EOR of Hydrocarbon Reservoirs: Potential Application, Prospects, Challenges and Governing Mechanisms. *Nanomaterials* **2022**, *12*, 4007. [CrossRef]
7. Tabaeh Hayavi, M.; Kazemzadeh, Y.; Riazi, M. Application of Surfactant-based enhanced oil recovery in carbonate Reservoirs: A critical review of the opportunities and challenges. *Chem. Phys. Lett.* **2022**, *806*, 139975. [CrossRef]
8. Mondal, M.C.; Uddin, H.M.W.; Progoti, Q.R.M.; Tushar, M.A.N.; Dutta, A.; Saif, T.; Malitha, S.B. Enhanced oil recovery via metal oxide nanoparticles: A review of recent advancements, core mechanisms, and future outlook. *Next Mater.* **2026**, *12*, 102004. [CrossRef]
9. Han, S.; Han, J.; Kim, J.W.; Lee, Y. Changes to interfacial characteristics by low salinity water/nanoparticle flooding in carbonate reservoir. *J. Pet. Sci. Eng.* **2022**, *208*, 109711. [CrossRef]
10. Rodriguez, E.; Roberts, M.R.; Yu, H.; Huh, C.; Bryant, S.L. Enhanced Migration of Surface-Treated Nanoparticles in Sedimentary Rocks. In Proceedings of the SPE Annual Technical Conference and Exhibition, New Orleans, LA, USA, 4–7 October 2009. [CrossRef]
11. Nourafkan, E.; Hu, Z.; Garum, M.; Esmaeili, H.; Wen, D. Nanomaterials for subsurface application: Study of particles retention in porous media. *Appl. Nanosci.* **2021**, *11*, 1847–1856. [CrossRef]
12. Wasan, D.; Nikolov, A.; Kondiparty, K. The wetting and spreading of nanofluids on solids: Role of the structural disjoining pressure. *Curr. Opin. Colloid Interface Sci.* **2011**, *16*, 344–349. [CrossRef]
13. Lau, H.C.; Yu, M.; Nguyen, Q.P. Nanotechnology for Oilfield Applications: Challenges and Impact. *J. Pet. Sci. Eng.* **2017**, *157*, 1160–1169. [CrossRef]
14. Zhao, J.; Wen, D. Pore-scale simulation of wettability and interfacial tension effects on flooding process for enhanced oil recovery. *RSC Adv.* **2017**, *7*, 41391–41398. [CrossRef]
15. Saien, J.; Moghaddamnia, F.; Bamdadi, H. Interfacial Tension of Methylbenzene–Water in the Presence of Hydrophilic and Hydrophobic Alumina Nanoparticles at Different Temperatures. *J. Chem. Eng. Data* **2013**, *58*, 436–440. [CrossRef]
16. Mohammed, M.; Babadagli, T. Wettability alteration: A comprehensive review of materials/methods and testing the selected ones on heavy-oil containing oil-wet systems. *Adv. Colloid Interface Sci.* **2015**, *220*, 54–77. [CrossRef]
17. Ogolo, N.A.; Olafuyi, O.A.; Onyekonwu, M.O. Enhanced Oil Recovery Using Nanoparticles. In Proceedings of the SPE Saudi Arabia Section Technical Symposium and Exhibition, Al-Khobar, Saudi Arabia, 8–11 April 2012. [CrossRef]
18. Hendraningrat, L.; Torsæter, O. Metal oxide-based nanoparticles: Revealing their potential to enhance oil recovery in different wettability systems. *Appl. Nanosci.* **2014**, *5*, 181–199. [CrossRef]
19. Hendraningrat, L.; Li, S.; Torsæter, O. Effect of Some Parameters Influencing Enhanced Oil Recovery Process using Silica Nanoparticles: An Experimental Investigation. In Proceedings of the SPE Reservoir Characterization and Simulation Conference and Exhibition, Abu Dhabi, United Arab Emirates, 16–18 September 2013. [CrossRef]
20. Ortega, D.J.; Kim, H.B.; James, L.A.; Johansen, T.E.; Zhang, Y. The Effectiveness of Silicon Dioxide SiO_2 Nanoparticle as an Enhanced Oil Recovery Agent in Ben Nevis Formation, Hebron Field, Offshore Eastern Canada. In Proceedings of the Abu Dhabi International Petroleum Exhibition & Conference, Abu Dhabi, United Arab Emirates, 7–10 November 2016. [CrossRef]
21. Roustaei, A.; Saffarzadeh, S.; Mohammadi, M. An evaluation of modified silica nanoparticles' efficiency in enhancing oil recovery of light and intermediate oil reservoirs. *Egypt. J. Pet.* **2013**, *22*, 427–433. [CrossRef]
22. Zhigarev, V.A.; Pryazhnikov, M.I.; Skorobogatova, A.D.; Pryazhnikov, A.I.; Minakov, A.V.; Zharkov, S.M. Comparing the effect of nanofluids in capillary imbibition with traditional displacing fluids. *Pet. Res.* **2025**, *10*, 432–442. [CrossRef]
23. Jafarbeigi, E.; Martyushev, D.A. Performance evaluation of a novel multifunctional synthetic smart nanofluid for oil recovery and asphaltene stability. *J. Mol. Liq.* **2025**, *438*, 128707. [CrossRef]
24. Nowrouzi, I.; Manshad, A.K.; Mohammadi, A.H. Effects of TiO_2, MgO, and γ-Al_2O_3 nano-particles in carbonated water on water-oil interfacial tension (IFT) reduction in chemical enhanced oil recovery (CEOR) process. *J. Mol. Liq.* **2019**, *292*, 111348. [CrossRef]
25. Amrouche, F.; Blunt, M.J.; Iglauer, S.; Aiouache, F.; Short, M. A novel hybrid enhanced oil recovery technique to enhance oil production from oil-wet carbonate reservoirs by combining electrical heating with nanofluid flooding. *Mater. Today Sustain.* **2024**, *27*, 100915. [CrossRef]
26. Assef, Y.; Pourafshary, P.; Hejazi, H. Controlling Interactions of Colloidal Particles and Porous Media During Low Salinity Water Flooding and Alkaline Flooding by MgO Nanoparticles. In Proceedings of the SPE EOR Conference at Oil and Gas West Asia, Muscat, Oman, 21–23 March 2016. [CrossRef]
27. Kandiel, Y.E.; Attia, G.; Metwalli, F.; Khalaf, R.; Mahmoud, O. Innovative Role of Magnesium Oxide Nanoparticles and Surfactant in Optimizing Interfacial Tension for Enhanced Oil Recovery. *Energies* **2025**, *18*, 249. [CrossRef]
28. Wayan Sutapa, I.; Wahid Wahab, A.; Taba, P.; La Nafie, N. Synthesis and Structural Profile Analysis of the MgO Nanoparticles Produced Through the Sol-Gel Method Followed by Annealing Process. *Orient. J. Chem.* **2018**, *34*, 1016–1025. [CrossRef]
29. Choudhury, S. A review of the sol-gel process and its application. *Int. Educ. Res. J.* **2024**, *10*, 122–126. [CrossRef]

30. Gurule, A.C.; Gaikwad, S.S.; Kajale, D.D.; Shinde, V.S.; Jadhav, G.R.; Gaikwad, V.B. Synthesis of magnesium oxide nanoparticles via hydrothermal and sol-gel methods: Charaterization and their application for H_2S and NO_2 gas sensing. *J. Indian Chem. Soc.* **2025**, *102*, 101496. [CrossRef]
31. Zhao, X.; Yang, H.; Wu, P.; Huang, X.; Wang, X. The preparation of MgO nanopowders synthesized an improved polyacrylamide gel method. *RSC Adv.* **2019**, *9*, 14893–14898. [CrossRef]
32. Ben Ahmed, H.; Pryazhnikov, M.; Pirogovskaya, J.; Zharkov, S.; Bril', I.; Minakov, A. Systematic Investigation of a Safer Polyacrylamide Gel Synthesis for MgO Nanoparticles with Tailored Properties. *Micro* **2026**, *6*, 39. [CrossRef]
33. Lee, J.; Kim, M. Polymeric Microfluidic Devices Fabricated Using Epoxy Resin for Chemically Demanding and Day-Long Experiments. *Biosensors* **2022**, *12*, 838. [CrossRef]
34. Pryazhnikov, A.I.; Vaganov, R.A.; Lubenets, S.S.; Yakimov, A.S.; Pryazhnikov, M.I.; Minakov, A.V. Systematic microfluidic study of the mechanisms of intensification of oil recovery by nanomodified surfactant-polymer compositions. *Microfluid. Nanofluidics* **2026**, *30*, 17. [CrossRef]
35. Pryazhnikov, A.I.; Vaganov, R.A.; Lubenets, S.S.; Yakimov, A.S.; Pryazhnikov, M.I.; Minakov, A.V. Microfluidic investigation of the efficiency of oil recovery by surfactant solutions modified with nanoparticles. *J. Mol. Liq.* **2025**, *438*, 128672. [CrossRef]
36. Peng, B.; Gao, H.; Liu, Q.; Yi, P.; Li, Y.; Liu, W.; Xu, Y. On the role of disjoining pressure in nanofluid-assisted enhanced oil recovery: A mini-review. *RSC Adv.* **2024**, *14*, 23322–23331. [CrossRef]

Disclaimer/Publisher's Note: The statements, opinions and data contained in all publications are solely those of the individual author(s) and contributor(s) and not of MDPI and/or the editor(s). MDPI and/or the editor(s) disclaim responsibility for any injury to people or property resulting from any ideas, methods, instructions or products referred to in the content.